Nanoscale

Accepted Manuscript

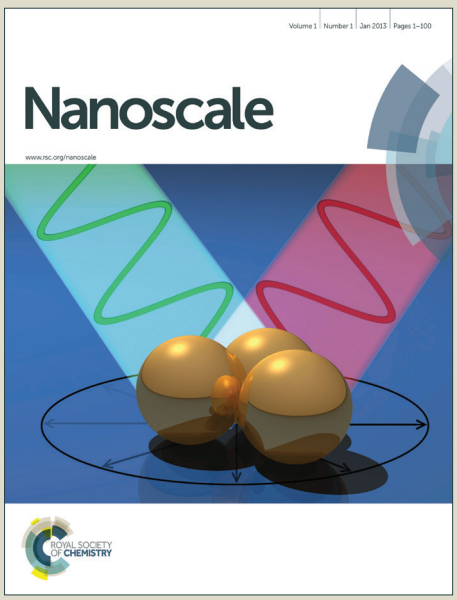

ROYAL SOCIETY OF CHEMISTRY

www.rsc.org/nanoscale

Journal Name

PAPER

Bamboo Leaves Derived Ultrafine Si Nanoparticles and Si/C Nanocomposites for High-performance Li-ion Battery Anodes

Received 00th January 20xx,
Accepted 00th January 20xx

DOI: 10.1039/x0xx00000x

www.rsc.org/

Lei Wang,[a] Biao Gao,[b] Changjian Peng,[a] Xiang Peng,[c] Jijiang Fu,[b] Paul K Chu[c] and Kaifu Huo*[a]

Silicon-based nanomaterials are promising anode materials in lithium-ion batteries (LIBs) due to high theoretical capacit of 4200 mAh g-1, more than 10 times that of commercial graphite. The Si nanoparticles (NPs) with diameter of or belo 10 nm generally exhibit enhanced lithium storage properties due to small size and large surface area. However, it is challenging to generate such ultrafine Si NPs by a facile and scalable method. This paper reports a scalable method t fabricate ultrafine Si NPs 5-8 nm in size from dead bamboo leaves (BLs) by thermally decomposing the organic matter followed by magnesiothermic reduction in the presence of NaCl as a heat scavenger. The ultrafine Si NPs show a high capacity of 1800 mAh g^{-1} at a 0.2 C (1 C=4200 mA g^{-1}) rate and are thus promising anode materials in lithium-ion batte To achieve better rate capability, the BLs-derived ultrafine Si NPs are coated by a thin amorphous carbon layer (Si@C) and then dispersed and embedded in a reduced graphene oxide (RGO) networks to produce Si@C/RGO nanocomposites b layer-by-layer assembly method. The double protection rendered by the carbon shell and RGO network synergistical yield structural stability, high electrical conductivity and stable solid electrolyte interface during Li insertion/extraction. The Si@C/RGO nanocomposites show excellent battery properties boasting high capability of 1400 mAh g^{-1} at a hig current density of 2 C and remarkable rate performance with capacity retention of 60 % when the current density is increased 20 times from 0.2 to 4 C. This work provides a simple, low cost, and scalable approach enabling the use of BLs waste as a sustainable source for the production of ultrafine Si NPs towards high-performance LIB

Introduction

Because of depletion of fossil fuels and increasing environmental pollution, much attention has been paid to rechargeable lithium-ion batteries (LIBs) due to their long cycling life as well as high energy densities for a large variety of applications such as portable electronics, electrical vehicles, and renewable energy storage. [1, 2] Silicon (Si) is a promising anode material for next generation LIBs because of its low Li-uptake potential and the large theoretical capacity of 4,200 mAh g^{-1}, which is ten times higher than that of commercial graphite anodes (372 mAh g^{-1}). [3-6] However, the practical application of Si as an anode material generally suffers from and extreme volume changes (> 300%) during Li alloying and dealloying processes, [7-9] which causes severe pulverization of active Si material, and the continuous formation of unstable solid electrolyte interphase (SEI) layer, [3, 10-12] resulting in rapid capacity fade of Si anodes upon cycling.

Reducing the size of Si to the nanoscale has bee demonstrated to be a promising strategy to improve the L storage performance of Si anodes because nanosized Si ca mitigate the physical strain and prevent pulverization of S active materials during lithiation/delithiation process.[13] I addition, nanosized Si permits rapid Li ion diffusion and electron transportation due to small size, thus leading to improved rate capability. In recent years, various morpholog of nano-Si such as Si nanoparticles (NPs),[13 14] nanowires,[11, 15] nanotubes,[16] hollow nanospheres,[17] and porous nanostructures[18, 19] have been designed and prepared towards high-performanc anode materials of LIBs. However, the Si NPs produced by the existing methods such as chemical vapor deposition, laser ablation [14, 20] are usually complex, costly, and energ demanding and are also difficult to scale up to cater to mass production. Moreover, Si NPs prepared via current metho are generally larger than 10 nm and have a broad particle size distribution. It has been reported that the Si NPs with the size o 10 nm or below generally exhibit enhanced lithium storage properties.[14] However, it is a challenge to generate ultrafine S nanoparticles with diameter below 10 nm by a simple, low cost, and scalable method towards practical LIB anodes.

Bamboo is one of the abundant natural resources occupying more than 14 million hectares in the tropical, subtropical, an temperate zones.[21] Bamboo is a Si accumulating plant which can act as the "natural factory" to absorb a vast quantity o Si from the soil in the form of water-soluble silicic acid and th

[a] Wuhan National Laboratory for Optoelectronics(WNLO), Huazhong University of Science and Technology, Wuhan 430074, China.
[b] The State Key Lab for Refractory and Metallurgy, Wuhan University of Science and Technology, Wuhan 430081, China.
[c] Department of Materials Science and Physics, City University of Hong Kong, Tat Chee Avenue, Kowloon, Hong Kong, China.
† E-mail: kfhuo@hust.edu.cn.
Electronic Supplementary Information (ESI) available: SEM and TG, for BLs, BET, TG and electrochemical characterizations for Si and Si@C/RGO. See DOI: 10.1039/c000000x/

convert into hydrate SiO_2 NPs in the roots, branches and leaves by biomineralization synthesis.[22] The content of biogenetic SiO_2 in the bamboo increases from roots to leaves. In the leaves, biogenetic SiO_2 NPs account for up to 13-41 wt% of the dried bamboo leaves (BLs), depending on the variety, climate, and geographic location.[23] Cultivation of bamboo generates a huge amount of waste BLs, which is an environmental nuisance. In Brazil, the waste BLs are about 190 kilotons per year. [24] In China, India and Japan, approximately 10 million tons of bamboo are harvested every year to generate a large amount of BLs. [21] The waste BLs are normally burnt in open landfill or limited to low value applications such as fertilizer and forage.[25] Consequently, more valuable utilization of this renewable biomass is highly required.

Herein, we report to recycle BLs as a sustainable resource to produce ultrafine Si NPs by thermally decomposing the organic matter, followed by magnesiothermic reduction in the presence of NaCl as a heat scavenger. The as-prepared Si NPs from the BLs have ultrafine sizes of 5-8 nm and a large surface area of 302 $m^2 g^{-1}$, which are otherwise difficult to produce on a large scale by the existing physical and chemical synthesis methods. [7, 20] The ultrafine Si NPs exhibit a high Li storage capacity over 1,800 mAh g^{-1} at a 0.2 C (1 C=4.2 A g^{-1}) rate, thus are promising anode materials for next-generation LIBs. To achieve a high power density and long cycle life, the BLs-derived ultrafine Si NPs are coated by a thin amorphous carbon layer (Si@C) and then dispersed and embedded in a reduced graphene oxide (RGO) networks to produce Si@C/RGO nanocomposites by a layer-by-layer assembly method. The C coatings suppress agglomeration of Si NPs and avoid direct exposure of the Si NPs to the electrolyte. Meanwhile, the elastic RGO sheets enable good dispersion for the Si@C NPs and guarantee high electrical conductivity of the electrode. As a result, the Si@C/RGO nanocomposites possess excellent Li storage properties boasting high capability of 1400 $mAhg^{-1}$ at a 2 C rate and remarkable rate performance with capacity retention of 60 % when the current density is increased 20 times from 0.2 to 4 C. This paper describes a simple, low cost, and scalable approach for ultrafine Si NPs production enabling the use of BLs waste as a sustainable source towards high-performance Si anodes for LIBs.

Experimental

Preparation of SiO_2 and Si NPs from dead BLs

The dead BLs used in this study were collected in September, 2013 from a bamboo garden in Wuhan National Laboratory for Optoelectronics, Huazhong University of Science and Technology (WNLO-HUST). Chlorhydric acid (HCl), hydrofluoric acid (HF) and sodium chloride (NaCl) were purchased from Sinopharm Chemical Reagent Co., Ltd. (Shanghai, China). Powdery magnesium (Mg, 99.5%), Tris(hydroxymethyl)aminomethane (Tris), and poly(diallyldimethylammonium) chloride (PDDA) were purchased from Aladdin Industrial Co. and dopamine hydrochloride was provided by Shanghai Demo Medical Tech. Co., Ltd. All the reagents were used without further purification.

The collected dead BLs were first washed with water seve times to remove dirt and dried at 100 ^oC overnight. The drie dead BLs were further leached in a 1 M HCl solution for 2 h t remove alkali impurities. After washing in water and drying the BLs were calcined in air at 700 ^oC for 2 h to remove organi components. Finally, white SiO_2 powders were produced.

Synthesis of ultrafine Si NPs from the as-produced SiO_2 wa conducted by a magnesiothermic reduction process. In a typical synthesis, BLs-derived SiO_2 (1 g), powdered Mg (1 g , and NaCl (8 g) were milled in an Ar-filled glove box and transferred to a corundum boat which was then quickly moved to a tube furnace. After purging three times with Ar to remove oxygen and moisture, the tube furnace was heated to 650 ^{o} and held at that temperature for 2 h. After the reaction, th samples were immersed into a 1 M HCl solution to selectivel dissolve magnesia (MgO), NaCl, and unreacted Mg, and the further immersed in 1M HF solution to remove residual Si Finally, the brown Si NPs were produced after removing the etchants by washing with DI water and alcohol followed by drying overnight under vacuum.

Preparation of Si@C and Si@C/RGO nanocomposites

A modified Hummers method was used to prepare the GO from natural graphite flakes.[26] The BLs-derived ultrafine Si NP were dispersed in 100 ml of the Tris-HCl buffer solutio (pH=8.5) and ultrasonically agitated for 20 min, and 0.2 g of dopamine chloride were added to a concentration of 2 mg ml Self-polymerization of dopamine on Si NPs was conducted at room temperature under continuous stirring for 4 h, resulting i the formation of polydopamine (PDA) coated Si NPs (Si@PDA). The as-produced Si@PDA NPs (0.4 g) wer filtered and rinsed with deionized (DI) water and further dispersed in 100 ml of PDDA (0.4 mg ml^{-1}) by vigorou ultrasonication to form positively charged Si@PDA-PDDA by absorbing PDDA cations. The excess PDDA was removed b several repeated centrifugation/wash/re-dispersion processes. The Si@PDA-PDDA NPs were carbonized in Ar to produce Si@C NPs. To prepare the Si@C/RGO nanocomposites, th positively charged Si@PDA-PDDA were dispersed in the GO aqueous solution (1 mg ml^{-1}) and assembled with negativ charged GO to form the Si@PDA/GO composites b electrostatic attraction under continuous magnetic stirring. Th as-prepared Si@PDA/GO composites were separated, dried and thermally treated at 800 ℃ under Ar/H_2 for 3 h to reduc GO and carbonize PDA to produce the Si@C/RGO nanocomposites.

Structural and Electrochemical Characterizations

The morphology, structure, and composition of Si, Si@C, and Si@C/RGO nanocomposites were characterized by X-ra diffraction (GAXRD, Philips X'Pert Pro), field-emission scanning electron microscopy (FE-SEM, FEI nanoSEM 450 transmission electron microscopy (TEM, FEI Titan 60-300 Cs). high-resolution TEM (HR-TEM, TITAN), energy-dispersive X-

ray spectroscopy (EDS, Oxford INCA 200) and Raman scattering (HR RamLab). The nitrogen adsorption and desorption isotherms were determined by the Brunauer-Emmett-Teller (BET) (Micrometrics, ASAP2010) method after degassing the samples at 383 K for 5 h. The Si content in the Si@C/RGO and SiO_2 in BLs were determined by thermogravimetric analysis (TGA, NETZSCH; TG 209 F3).

The electrochemical properties of the BLs-derived Si NPs and Si@C/RGO nanocoposites were studied using 2025 coin cells. To prepare the working electrodes, Si, Si@C NPs, or Si@C/RGO nanocomposites, sodium carboxyl methyl cellulose (Na-CMC, Sigma Aldrich), and carbon black (conducting agent) in a composition of 70, 10 and 20 wt%, respectively, were mixed in distilled water to form a slurry and then pasted on a copper foil. The mass loading of Si active materials is typically about 0.5 mg/cm^2. The electrolyte was a 1 M solution of LiPF6 in a 1:1 vol/vol mixture of ethylene carbonate (EC) and diethyl carbonate (DEC) with 10 wt.% fluoroethylene carbonate (FEC, 98 % purity, Aladdin) as an additive. A Celgard 2400 film was used as the separator and pure Li foil as the counter electrode. The 2025 cells were assembled in an argon-filled glove box (oxygen and H_2O content < 1 ppm). The charging and discharging measurement of the batteries were conducted on MTI automatic battery cyclers with the voltage cut-off between 0.01 and 1 V vs. Li/Li$^+$. The specific capacity was calculated based on the mass loading of Si in the electrode. Cyclic voltammetry (CV) was conducted on the CHI 660e electrochemical workstation and the electrochemical impedance spectra (EIS) were acquired on an Autolab electrochemical workstation between 10 mHz and 0.1 MHz.

Results and discussion

Schematic 1 shows the flow diagram for the production of ultrafine Si NPs from dead BLs and further modification to produce Si@C/RGO nanocomposites for LIBs applications. The ultrafine Si NPs are produced by magnesiothermic reduction of the BLs-derived mesoporous SiO_2 NPs at 650 ^oC under Ar using NaCl as a heat scavenger. To prepare the Si@C/RGO nanocomposites, the ultrafine Si NPs are first modified by PDDA cation surfactant to be positively charged, and then dispersed in a negatively charged GO aqueous solution under continuous magnetic stirring to produce the Si@PDA/GO nanocomposites by electrostatic assembly. The resulting Si@PDA/GO are thermally treated under Ar/H_2 to reduce GO and carbonize PDA to produce the Si@C/RGO nanocomposites.

Fig. 1a is an optical photograph of the dead BLs collected from the bamboo garden of WNLO-HUST, Wuhan, China. They have a yellow-brown color and the typical size is about 1.5 cm x 9 cm. The FE-SEM images (Fig. 1b and c) indicate that the NPs with a size of about 40-50 nm are distributed in the BLs. The elemental map (Fig. 1d) obtained by EDS further indicates that Si element is uniform distributed in the skeleton of the organic components of the BLs. Similar to rice husks,[27] BLs contain metallic components and so we first immerse the BLs in a diluted HCl solution to remove the metallic elements. This HCl-leaching step avoids the formation of glassy state silicate while removing the organic matters by burning in Air.[27-28] After HCl-leaching, the BLs become darker (Fig. S1†,ESI). The thermogravimetric (TG) curve in Fig. S2†(ESI) reveals that the SiO_2 weighs about 42 % of the total mass of the HCl-leached BLs. The mass decrease in the temperature ranges from 150-300, 300-450 and 450-600 ℃ can be attributed to decomposition of cellulose, semi-cellulose, and lignin and carbonous residues of the dead BLs, respectively.[27]

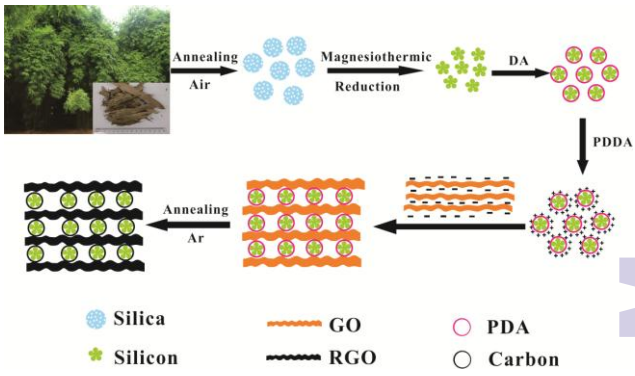

Schematic 1 Schematic illustration of the production of ultrafine Si NPs from dead BLs and fabrication of the Si@C/RGO nanocomposites.

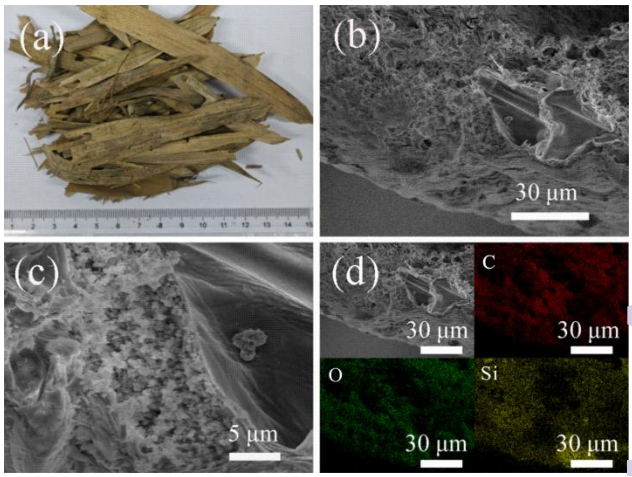

Fig. 1 Optical image (a), low- and high-magnification cross-section SEM images (b, c) and EDS mapping (d) of dead BLs.

Fig. 2a depicts the SEM image of the SiO_2 NPs derived from the dead BLs revealing that SiO_2 retains the original morphology in the BLs with a uniform size of about 40-50 nm. It is further confirmed by the transmission electron microscopy (TEM) image in Fig. 2b. The EDS result (inset in Fig. 2b) indicates the NPs consist of Si and O elements. The C and Cu peaks are attributed to the Cu grid and C membrane used in TEM examination. The X-ray diffraction (XRD) pattern (Fig. S3†, ESI) shows a broad peak at around $2\Theta = 22.5°$, suggesting that the SiO_2 NPs derived from BLs are amorphous.[27, 28] The high resolution TEM (HR-TEM) image (Fig. 2c) further

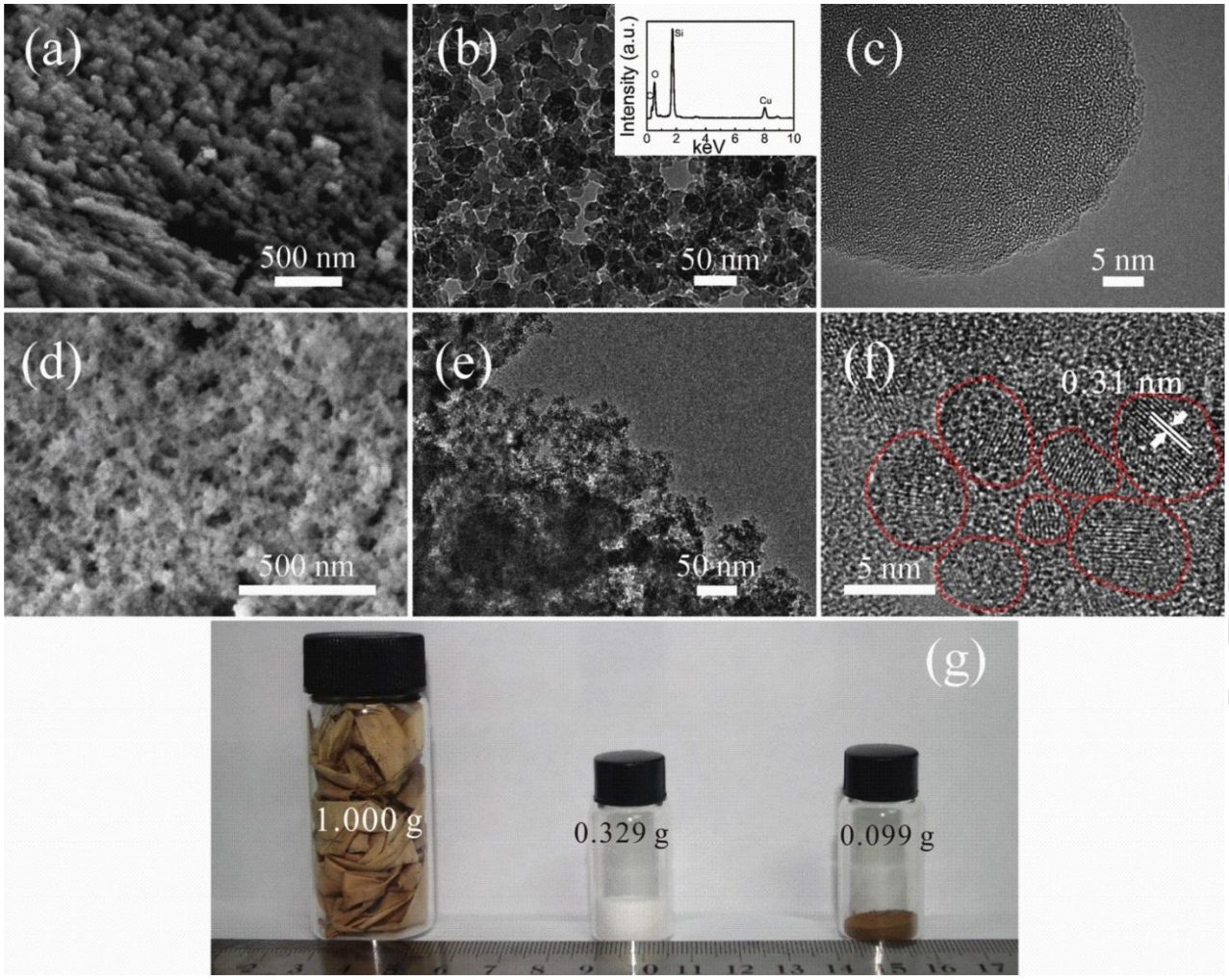

Fig. 2 (a-c) SEM, TEM, and HR-TEM images of SiO_2 NPs derived from the dead BLs. (d-f) SEM, TEM, and HR-TEM images of the ultrafine Si NPs obtained by Mg reduction of SiO_2 NPs (a). The closed red curves in (f) represent small Si nanocrystallines. (g) Visual comparison of dead BLs and BLs-derived SiO_2 and Si NPs stored in glass vials.

confirms the amorphous characteristics of the SiO_2 NPs derived from BLs. The nitrogen adsorption-desorption experiments yield an isotherm that corresponds to type IV with a distinct hysteresis loop at a high relative pressure (P/P_0), indicating that the SiO_2 derived from dead BLs is mesoporous (Fig. S4a†,ESI). The SiO_2 NPs derived from BLs exhibited higher BET surface (329 m^2 g^{-1}) and larger pore volume (0.53 cm^3 g^{-1}) compared with mesoporous SiO_2 derived from rice husks. [28, 29] The Barrett-Joyner-Halenda (BJH) pore-size distribution of the BLs-derived SiO_2 shows several peaks at 3-8 nm, further corroborating the presence of mesopores (Fig. S4c†, ESI,).

In the industry, carbothermal reduction of SiO_2 is the primary method for metallurgical Si production from SiO_2. However, this process is impractical to synthesize Si nanostructures due to the high processing temperature (over 2000 ^oC). [30] In the effort to convert the BLs-derived SiO_2 NPs into Si NPs, magnesiothermic reduction [30, 31] is conducted at 650 ^oC by Reaction (1):

$SiO_2(s) + Mg(g) \rightarrow Si(s) + 2MgO(s)$ Reaction (1)

$2Mg(g) + Si(s) \rightarrow Mg_2Si(s)$ Reaction (2)

Considering the Reaction (1) is highly exothermic, in a typical synthesis, the magnesium (Mg) powder as a reducing agent is usually located by a certain distance from the SiO_2 powder in a reactor, which evaporates and then diffuses to reduce adjacent SiO_2 precursors.[27, 31, 32] However, this vapor-transport reaction inevitably suffers from reaction inhomogeneity. The as-reduced Si near the Mg source can be further converted into Mg_2Si by Reaction (2), while SiO_2 far from the Mg source may not be involved in the magnesiothermic reduction, resulting in a limited yield and inhomogeneity. Herein, we introduce NaCl as a heat scavenger and conduct the magnesiothermic reaction by premixing Mg, SiO_2, and NaCl together to improve the reaction yield and homogeneity.[30] NaCl can effectively consume the heat generated by the exothermic Mg reduction reaction (Reaction (1)) and halt the reaction at temperature higher than 801 ^oC via fusion of NaCl, thus preventing the collapse of the nanoporosity SiO_2 precursor and agglomeration of Si into large crystals. Therefore, the nanosized Si with a uniform morphology can be prepared with a high yield after NaCl, Mg...

Mg_2Si and unreacted Mg are removed. Fig. 2d is the SEM image of as-produced Si powders, revealing that the Si powers have the similar overall morphology to the original SiO_2 powers. However, TEM image (Fig. 2d) shows that the as-reduced Si powers are composed of ultrafine Si NPs with a size of 5-8 nm and they are interconnected forming a highly nanoporous interconnected network. This uniform Si NPs with small size of 5-8 nm are difficult to produce on a large scale by common physical and chemical methods.[14, 33] The lattice-resolved HR-TEM image (Fig. 2f) further reveals that the ultrafine Si NPs are nanocrystallites with distinct lattice fringes of 0.31 nm, corresponding to the Si (111) planes of cubic phase. The XRD pattern (Fig. S5†, ESI) indicates that the diffraction peaks are ascribed to the cubic phase of Si (JCPDS: 77-2111). The Raman shifts at 517 cm^{-1} is ascribed to Raman mode of crystalline Si.[34] The BET results (Fig. S4b†, ESI) show that the surface area and pore volume of the ultrafine Si NPs are 302 $m^2 g^{-1}$ and 0.53 $cm^3 g^{-1}$, respectively. Assuming a density of 2.33 g cm^{-3} for Si, a particle size of about 8 nm can be calculated from the ultrafine nano-Si according to the BET surface area and it is consistent with SEM and TEM results. The ultrafine Si NPs prepared from BLs derived SiO_2 can be attributed to the mesoporous structure of SiO_2 NPs with large surface area and heat-scavenging effect of NaCl during Mg reduction reaction of mesoporous SiO_2 NPs. As shown in Fig. S6†(ESI), without adding NaCl as the heat-scavenger, only large Si particles sintered together with a size of ten micrometers are prepared. The dramatic morphological change observed from the Si product with or without NaCl additive may be due to the different local reaction temperature. It has been reported that the temperature during Mg reduction of SiO_2 can reach 1720 ^oC due to the large heat release from the highly exothermic reaction,[35] which is much higher than the set temperature of 650 ^oC. Such high local temperature can collapse the architecture of the nanosized SiO_2 precursor and fuse and agglomerate the as-synthesized Si into large crystals, resulting in the formation of bulk Si (Fig. S6†, ESI). The as-reduced Si NPs have a much smaller size of 5-8 nm in comparison with pre-reduction SiO_2 particles of 40-50 nm, as Fig. 2b and e revealed.

The size change after magnesiothermic reduction could attribute to the breakdown of as-reduced mesoporous Si NPs during magnesiothermic reduction and ultrasonication for TEM characterization due to the reduced mechanical integrity of porous Si NPs in comparison to the pre-reduction SiO_2 NPs. This assumption is also supported by the fact that the as-reduced Si NPs have the similar specific surface area and pore volume compared to original mesoporous SiO_2 powers (Fig. S4 †, ESI). Moreover, the porous interconnected Si powers have the overall morphology similar to original mesoporous SiO_2 NPs, as Fig. 2a and d suggested. A visual comparison of the dead BLs, mesoporous SiO_2, and ultrafine Si NPs stored in glass vials is illustrated in Fig. 2g, revealing that ultrafine Si NPs with high yield of approximately 10 % can be produced from dead BLs.

The above-mentioned results indicate that ultrafine Si NPs 5-8 nm in size can be produced on a large scale from BLs by HCl leaching, thermally decomposing the organic matter, and subsequent Mg reduction in the presence of NaCl as a heat scavenger. The ultrafine Si NPs are promising anode materi for next-generation LIBs due to small size and large surfac area. However, owing to the intrinsically low conductivit (about 10^{-3} S m^{-1}) and inevitable electrochemical sintering of Si NPs during charging and discharging, the ultrafine Si NP may suffer from poor rate capability as following Fig. 4e revealed, thus potentially limiting their application as LIB anodes. In order to achieve high power density and long cycle life, the as-prepared ultrafine Si NPs are further converted int Si@C/RGO nanocomposites. The Si@C/RGO nanocomposites are expected to have superior Li storage properties because the RGO and C layers could work synergistically to yield high electrical conductivity and structural stability during L insertion/extraction.

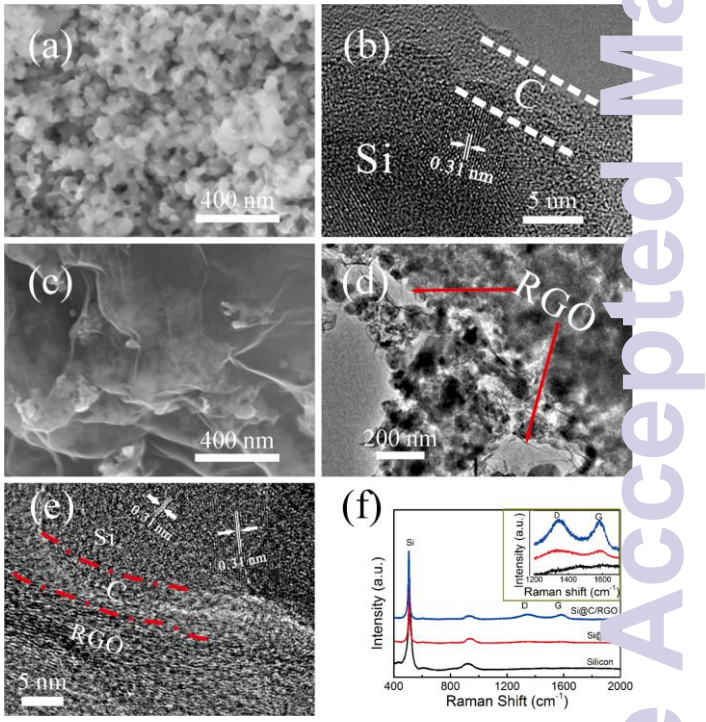

Fig. 3 (a) SEM and HR-TEM of Si@C NPs. (c-e) SEM,TEM, and HR-TEM images of Si@C/RGO nanocomposites, showing Si@C NPs are well dispersed and wrapped in the networks made fro thin RGO nanosheets. (f) Raman shifts of Si, Si@C NPs and Si@C/RGO nanocomposites.

PDA is chosen as a precursor of the C coating sinc dopamine polymerization yields a highly conformal polymer layer with a tunable thickness.[36] The Si@PDA NPs ar carbonized at 800 ^oC under Ar to produce Si@C NPs. The SEM image in Fig. 3a discloses that the size of the Si@C NPs is 40 60 nm and they are much larger than the size of ultrafine S NPs, suggesting possible formation of pomegranate-shape carbon coated Si NPs in which some interconnected ultrafine S NPs are coated by a thin carbon shell. The TEM image in Fig. 3b further demonstrates that several aggregated Si NPs are

covered by a thin carbon layer with a thickness of 3-5 nm. The Si@C/RGO nanocomposites are fabricated by reducing GO and carbonizing PDA of the Si@PDA/GO nanocomposites under Ar/H_2 at 800 °C. Fig. 3c and d show the SEM and TEM images of the Si@C/RGO nanocomposites, indicating Si@C NPs are well dispersed and wrapped in the networks made from thin RGO nanosheets. The HR-TEM image in Fig. 3e further confirms the Si@C/RGO nanocomposites. The EDS mapping (Fig. S7†, ESI) shows that Si is uniformly distributed in C consisting of a C coating and RGO. The XRD patterns shown in Fig. S5†(ESI) indicate that Si in Si@C/RGO nanocomposites still retains the crystalline structure. No obvious peaks corresponding to carbon are detected by XRD, suggesting that carbon is not well crystallized. The Raman spectra (Fig. 3f) of Si@C and Si@C/RGO nanocomposites show two characteristic peaks at ~1360 and ~1580 cm^{-1}, corresponding to the D band and G band of graphite, respectively.[35] The main peak at 517 cm^{-1} arises from the crystalline Si structure.[34] Since the carbon coating on Si@C is very thin (about 3-5 nm) and the intensity of main peak of Si is very strong, the D and G bands of carbon for Si@C are not clearly identified. However, the intensity of D band and G band of the Si@C/RGO nanocomposites increases due to the presence of RGO. The TG curves of Si@C and Si@C/RGO (Fig. S8†) indicate that the C coating and RGO contribute about 6.9% and 11.9%, respectively, and so the weight of Si in Si@C/RGO nanocomposites is 82.2%.

The Li storage properties of the ultrafine BLs-derived Si NPs and Si@C/RGO nanocomposites are investigated in an electrolyte consisting of 1:1 vol/vol mixture of ethylene carbonate (EC) and diethyl carbonate (DEC) with 10 wt.% FEC as an additive. Fig. 4a shows the discharging-charging profiles of the Si NPs in a coin-type half-cell for the 1st, 2nd, 5th, 50th, and 100th galvanostatic charging/discharging cycles in the voltage range between 0.01 and 1 V versus Li^+/Li. For the first cycle at a rate of C/20 (1 C=4200 mA g^{-1}), the discharge (lithiation) and charge (delithiation) capacity of the Si NPs reaches 2983 and 2590 mAh g^{-1}, respectively, meaning an initial columbic efficiency of 87 %, which is higher than that of other Si-based anodes.[18, 37-39] The long flat plateau at ~0.09 V (vs. Li/Li^+) in the first discharge curve is indicative of the alloying reaction between nanocrystalline Si and Li. After the first lithiation/delithiation process, crystalline Si turns to amorphous phase. The cyclic voltammetry (CV) curve (Fig. 4b) shows a peak at ~0.8 V in the first cathodic branch, which is absent from the following cycles, suggesting the formation of SEI films on the surface of the electrode due to the decomposition of the electrolyte.[27] This is the main reason for the initial irreversible capacity loss. The discharge capacity of the ultrafine Si NPs decreases from the 2nd cycle and then slightly increases at a 0.2 C rate (Fig. 4a), suggesting a gradual activation process on the electrode consisting of a highly porous interconnected network of ultrafine Si NPs.[17, 31, 40] This gradual activation process of Si NPs is also indicated by the increase in the CV peak intensity (Fig. 4b) corresponding to lithiation and delithiation in the first 10 cycles before stabilization and it is also observed from other Si-based anodes.[5, 31] In the cathodic branch of the CV curves, the peak at 0.17 V corresponds to the conversion of amorphous Si to the Li_xSi phase. The two peaks at 0.42 and 0.54 V in the anodic branch correspond to delithiation of Li_xSi to amorphous Si.[5, 7] The BLs-derived Si NPs exhibit good cycle stability and high specific capacity of 1,800 and 1,200 mAh g^{-1} at 0.2 C and 0.5 C rates after 100 cycles (Fig. S9†), which are 4.8 and 3.2 times larger than that of the theoretical capacity of graphite. The areal and volumetric capacity of the electrodes are 0.90 mA h cm^{-2} and 600 mA h cm^{-3}, respectively. The high coulombic efficiency and cycle stability of the ultrafine NPs may be attributed to the highly porous interconnected network consisting of ultrafine Si NPs and addition of FEC to the electrolyte, which enlarge the interface between the active Si and electrolyte and facilitate the formation of a stable SEI.

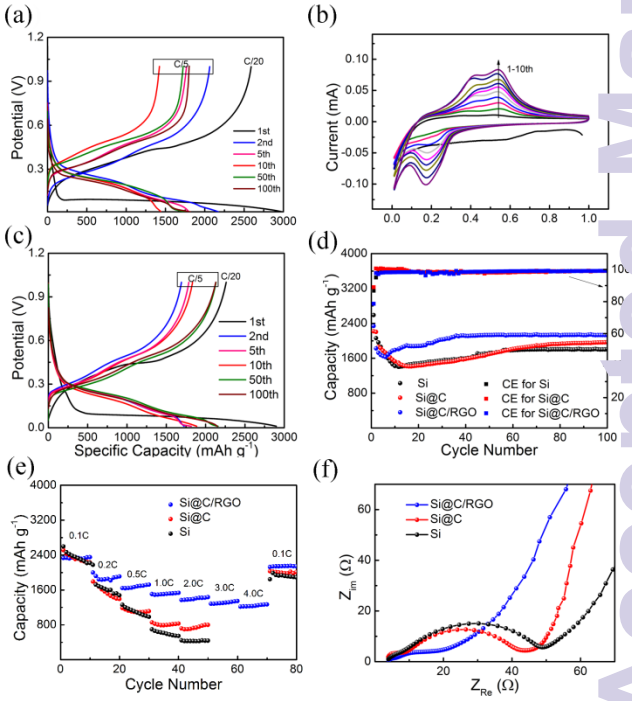

Fig. 4 Electrochemical characterization of the Si, Si@C, and Si@C/RGO anodes: (a-b) Galvanostatic charging – discharging voltage profile and CV results obtained at a scanning rate of 0.1 V/s from the Si NPs as anodes. (c) Galvanostatic charging discharging voltage profile of the Si@C/RGO anodes. (d) Discharge capacity versus cycle number for the Si, Si@C and Si@C/RGO anodes at a rate of 0.2 C. (e-f) Rate performance and EIS after 50 cycles for the Si, Si@C, and Si@C/RGO anodes. All the capacities are calculated based on the mass loading of active Si material.

Although the BLs-derived Si NPs exhibit good Li storage activity, the rate capability is unsatisfactory. As shown in Fig. 4e, the capacity drops sharply from 2,200 to 540 mAh g^{-1} when the current density is increased from 0.1 to 1 C, indicating poor rate capability. Moreover, electrochemical polarization of ultrafine NPs is very strong as suggested by Fig. 2a. The poor rate capability and strong polarization of the BLs-derived

ultrafine Si NPs may be attributed to the intrinsically low conductivity and inevitable electrochemical sintering during charging and discharging. [39] To achieve high power density and long cycle life, the Si@C/RGO nanocomposites are prepared. Fig. 4c depicts the discharging-charging profiles of the Si@C/RGO nanocomposites in the 1st, 2nd, 5th, 50th, and 100th galvanostatic charging/discharging cycles in the voltage range between 0.01 and 1 V versus Li/Li^+. Similar to the ultrafine Si NPs, the Si@C/RGO nanocomposites also show a gradual activation process. However, the Si@C/RGO nanocomposites exhibit lower polarization and higher specific capacity compared to the pristine Si NPs. The first lithiation and delithiation capacity of the Si@C/RGO nanocomposites is 2,678 and 2,106 mAh g^{-1} at a current density of 210 mA g^{-1} (C/20), meaning that the first coulombic efficiency is 79%, which is smaller than that of the ultrafine Si NPs. The reduced first coulombic efficiency should attribute to increased formation of the nonconducting SEI on the RGO network with a large surface area. [39, 41] The discharging capacity curves of the Si, Si@C, and Si@C/RGO nanocomposites versus cycle number are shown in Fig. 4d. After 100 cycles, the Si@C/RGO nanocomposites still retain a reversible capacitance of 1,900 mAh g^{-1} at a 0.2 C rate, whereas the Si NPs only show a specific capacity of 1,800 mAh g^{-1}. Furthermore, the Si@C/RGO nanocomposites exhibit a significantly improved rate capability compared to Si and Si@C NPs. As shown in Fig. 4d, the Si@C/RGO nanocomposites have a higher capacity than Si and Si@C NPs under higher current densities. At a high current density of 8.4 A g^{-1} (2 C), the Si@C/RGO nanocomposites have a favorable capacity of 1,400 mAh g^{-1}, whereas the ultrafine Si NPs only retain a specific capacity of 430 mAh g^{-1}. Even at a larger current density of 16.8 A g^{-1} (4 C), the Si@C/RGO nanocomposites deliver a high capacity of 1200 mAh g^{-1} that is about 3.2 times bigger than the theoretical capacity of graphite. The capacity retention of the Si@C/RGO nanocomposites is 60 % when the current density is increased 20 times from 0.2 to 4 C. Moreover, after the high rate measurements for more than 60 cycles, the reversible capacity of the Si@C/RGO nanocomposites under 0.1 C recovers to the primitive values at 0.1 C, implying excellent reversibility and rate capability. To further understand the mechanism of the improved battery performance of the Si@C/RGO, electrochemical impedance spectroscopy (EIS) is performed after the 50th cycle on the electrodes with the full delithiation state. The Nyquist plots of the Si, Si@C, and Si@C/RGO are presented in Fig. 4f and the equivalent circuit is shown in Fig. S10†(ESI). The depressed semicircles in the high-frequency region represent the overlap of the resistance of the SEI film and charge transfer resistance, whereas the straight lines in the low-frequency region correspond to diffusion of lithium ions. The SEI film resistances (R_{SEI}) for the electrodes of Si, Si@C, and Si@C/RGO are estimated to be 13.27, 7.87 and 3.97 Ω, respectively and the charge transfer resistances (R_{ct}) are calculated to be 40.16, 32.81 and 8.17 Ω, respectively. R_{SEI} for Si@C/RGO is smaller than that of Si, suggesting that the SEI at Si@C/RGO is thinner and more stable than the Si NPs. Moreover, R_{ct} of the Si@C/RGO is lower than one for the Si NPs, suggesting faster electron transfer due to the high conductivity. These results indicate that the Si@C/RGO nanocomposites have better rate capability and reversible capacity in comparison with the ultrafine Si and Si@C NPs. The excellent Li storage properties of the Si@C/RGO nanocomposites arise from the double protection from the C shell and RGO network thus giving rise to efficient electron and ion transport and eventually large capacity, high rate capability and superior cycling performance.

Conclusions

A simple, low cost, and scalable approach for ultrafine Si NPs with the size below 10 nm is a challenge for Si fabrication and applications. This ultrafine Si nanoparticles with the diameters of 5-8 nm were produced on a large scale from dead bamboo leaves by Mg reduction of biogenetic SiO_2 in BLs using NaCl as a heat scavenger. The ultrafine Si NPs are interconnected to form a porous network and have favourable Li storage properties boasting a capacity that is more than 1,800 mAh g^{-1} after 100 cycles at a 0.2 C rate. The materials are thus promising as anode materials in next-generation LIBs. To achieve a better rate capability, the BLs-derived ultrafine Si NPs are further converted into Si@C/RGO nanocomposites by the layer-by-layer assembly method. The double protection rendered by the C shell and RGO minimizes volume changes, avoids direct contact between Si and electrolyte, and yields high electrical conductivity. The Si@C/RGO nanocomposites thus have excellent battery properties as anodes of LIBs. At a larger current density of 16.8 A g^{-1} (4 C), the Si@C/RGO nanocomposites retain the reversible capacity of over 1200 mAh g^{-1}. In addition, the capacity retention of the Si@C/RGO nanocomposites is 60% when the rate is increased 20 times from 0.2 to 4 C, implying excellent reversibility and rate capability. This study provides a simple and scalable approach for ultrafine Si NPs production and demonstrates the large potential of using waste BLs as a sustainable source towards high-performance anodes for LIBs.

Acknowledgements

This work was financially supported by Fundamental Research Funds for the Central Universities (HUST: 0118187099), Outstanding Young and Middle-aged Scientific Innovation Team of Colleges and Universities of Hubei Province (T201402), Applied Basic Research Program of Wuhan City (2013011801010598) and City University of Hong Kong Strategic Research Grant (SRG) No. 7004188, and Guangdong - Hong Kong Technology Cooperation Funding Scheme (TCFS) GHP/015/12SZ. The authors thank the facility provided by the Nanodevices and Characterization Center of WNLO-HUST.

Notes and references

1 1. J. M. Tarascon and M. Armand, *Nature*, 2001, **414**, 359-367.

2 2. M. S. Whittingham, *Chem. Rev.*, 2004, **104**, 4271-4301.
3 3. W. J. Lee, T. H. Hwang, J. O. Hwang, H. W. Kim, J. Lim, H. Y. Jeong, J. Shim, T. H. Han, J. Y. Kim, J. W. Choi and S. O. Kim, *Energy Environ. Sci.*, 2014, **7**, 621-626.
4 4.N. Liu, Z. Lu, J. Zhao, M. T. McDowell, H.-W. Lee, W. Zhao and Y. Cui, *Nat. Nanotech.*, 2014, **9**, 187-192.
5 5.T. D. Hatchard and J. R. Dahn, *J. Electrochem. Soc.*, 2004, **151**, A838-A842.
6 6.J. P. Maranchi, A. F. Hepp and P. N. Kumta, *Electrochem. Solid-State Lett.*, 2003, **6**, A198-A201.
7 7.B. M. Bang, H. Kim, H.-K. Song, J. Cho and S. Park, *Energy Environ. Sci.*, 2011, **4**, 5013-5019.
8 8.H. Kim, B. Han, J. Choo and J. Cho, *Angew. Chem. Int. Ed.*, 2008, **47**, 10151-10154.
9 9.M. N. Obrovac and L. J. Krause, *J. Electrochem. Soc.*, 2007, **154**, A103-A108.
10 10.M. H. Park, M. G. Kim, J. Joo, K. Kim, J. Kim, S. Ahn, Y. Cui and J. Cho, *Nano Lett.*, 2009, **9**, 3844-3847.
11 11.Y. Yao, N. Liu, M. T. McDowell, M. Pasta and Y. Cui, *Energy Environ. Sci.*, 2012, **5**, 7927-7930.
12 12.Z.-J. Han, N. Yabuuchi, K. Shimomura, M. Murase, H. Yui and S. Komaba, *Energy Environ. Sci.*, 2012, **5**, 9014.
13 13.X. H. Liu, L. Zhong, S. Huang, S. X. Mao, T. Zhu and J. Y. Huang, *ACS Nano*, 2012, **6**, 1522-1531.
14 14.H. Kim, M. Seo, M. H. Park and J. Cho, *Angew. Chem. Int. Ed.*, 2010, **49**, 2146-2149.
15 15.H. T. Nguyen, F. Yao, M. R. Zamfir, C. Biswas, K. P. So, Y. H. Lee, S. M. Kim, S. N. Cha, J. M. Kim and D. Pribat, *Adv. Energy Mater.*, 2011, **1**, 1154-1161.
16 16.J. K. Yoo, J. Kim, Y. S. Jung and K. Kang, *Advanced materials*, 2012, **24**, 5452-5456.
17 17.W. Li, Z. Li, W. Kang, Y. Tang, Z. Zhang, X. Yang, H. Xue and C.-S. Lee, *J. Mater. Chem. A*, 2014, **2**, 12289-12295.
18 18.C. Y. Du, C. H. Gao, G. P. Yin, M. Chen and L. Wang, *Energy Environ. Sci.*, 2011, **4**, 1037-1042.
19 19.Z. Zhang, Y. Wang, W. Ren, Q. Tan, Y. Chen, H. Li, Z. Zhong and F. Su, *Angew. Chem. Int. Ed.*, 2014, **53**, 5165-5169.
20 20.M. Y. Ge, J. P. Rong, X. Fang, A. Y. Zhang, Y. H. Lu and C. W. Zhou, *Nano Res.*, 2013, **6**, 174-181.
21 21.M. Umemura and C. Takenaka, *Ecol. Res.*, 2014, **29**, 501-510.
22 22.H. A. Currie and C. C. Perry, *Ann. Bot.-london*, 2007, **100**, 1383-1389.
23 23.K. W. Kow, R. Yusoff, A. R. A. Aziz and E. C. Abdullah, *J. Non-cryst. Solids*, 2014, **386**, 76-84.
24 24.M. T. Grombone-Guaratini, M. Gaspar, V. F. Oliveira, M. Torres, A. do Nascimento and M. P. M. Aidar, *New Zeal. J. Bot.*, 2013, **51**, 275-285.
25 25.Y. Zhang, W. Xu, X. Wu, X. Zhang and Y. Zhang, *Food Addit. Contam.*, 2007, **24**, 242-251.
26 26.N. I. Kovtyukhova, P. J. Ollivier, B. R. Martin, T. E. Mallouk, S. A. Chizhik, E. V. Buzaneva and A. D. Gorchinskiy, *Chem. Mater.*, 1999, **11**, 771-778.
27 27.D. S. Jung, M. H. Ryou, Y. J. Sung, S. B. Park and J. W. Choi, *Proc. Natl. Acad. Sci. U. S. A.*, 2013, **110**, 12229-12234.
28 28.N. Liu, K. Huo, M. T. McDowell, J. Zhao and Y. Cui, *Sci. Rep.*, 2013, **3**, 1919-1925.
29 29.T.-H. Liou, *Mater. Sci. Eng. A*, 2004, **364**, 313-323.
30 30.I. M. M. Nagamori, A. Claveau, *Metall. Trans. B*, 1986, **17**, 503-514.
31 31.Z. Favors, W. Wang, H. H. Bay, Z. Mutlu, K. Ahmed, C. Liu, M. Ozkan and C. S. Ozkan, *Sci. Rep.*, 2014, **4**, 5623-5629.
32 32.Z. H. Bao, M. R. Weatherspoon, S. Shian, Y. Cai, P. D. Graham, S. M. Allan, G. Ahmad, M. B. Dickerson, B. C. Church, Z. T. Kang, H. W. Abernathy, C. J. Summers, M. D. Liu and K. H. Sandhage, *Nature*, 2007, **446**, 172-175.
33 33.A. Magasinski, P. Dixon, B. Hertzberg, A. Kvit, J. Ayala and G. Yushin, *Nat. Mater.*, 2010, **9**, 461-461.
34 34.Y. Ru, D. G. Evans, H. Zhu and W. Yang, *RSC Adv.*, 2013, **4**, 71-75.
35 35.C. W. Won, H. H. Nersisyan and H. I. Won, *Sol. Energ. Mater. Sol. C.*, 2011, **95**, 745-750.
36 36.H. Lee, S. M. Dellatore, W. M. Miller and P. B. Messersmith, *Science*, 2007, **318**, 426-430.
37 37.M. Gauthier, D. Mazouzi, D. Reyter, B. Lestriez, P. Moreau, D. Guyomard and L. Roué, *Energy Environ. Sci.*, 2013, **6**, 2145-2155.
38 38.H. Li, C. Lu and B. Zhang, *Electrochim. Acta*, 2014, **120**, 96-101.
39 39.H.-C. Tao, X.-L. Yang, L.-L. Zhang and S.-B. Ni, *Ionics*, 2014. DOI: 10.1007/s11581-014-1218-9
40 40.C. Wang, Y.-S. Chui, R. Ma, T. Wong, J.-G. Ren, Q.-H. Wu, X. Chen and W. Zhang, *J. Mater. Chem. A*, 2013, **1**, 10092-10098.
41 41.X. Zhou, Y.-X. Yin, L.-J. Wan and Y.-G. Guo, *Adv. Energy Mater.*, 2012, **2**, 1086-1090.